Controlling the Thermoelectric Properties of Nb-doped TiO_2 Ceramics through Engineering Defect Structures

*Xiaodong Liu,[†] Demie Kepaptsoglou,[‡] Zhaohe Gao,[†] Andrew Thomas,[†] Krishnendu Maji,[ǂ] Emmanuel Guilmeau,[ǂ] Feridoon Azough,[†] Quentin M. Ramasse[‡] and Robert Freer[†]**

[†]Department of Materials, University of Manchester, Manchester M13 9PL, United Kingdom

[‡] SuperSTEM Laboratory, STFC Daresbury Campus, Daresbury WA4 4AD, United Kingdom

[ǂ] CRISMAT, ENSICAEN, UNICAEN, Normandie Univ, CNRS, 14000 Caen, France

ABSTRACT:

Donor-doped TiO_2 ceramics are promising high temperature oxide thermoelectrics. Highly dense $(1-x)TiO_2$ - xNb_2O_5 ($0.005<x<0.06$) ceramics were prepared by a single step, mixed oxide route under reducing conditions. The microstructures contained polygonal-shaped grains with uniform grain size distributions. Sub-grain structures were formed in samples with low Nb contents by the interlacing of rutile and higher order Magnéli phases, reflecting the high density of shear planes and oxygen vacancies. Samples prepared with higher Nb content showed no sub-grain structures but high-densities of planar defects, and lower concentrations of oxygen vacancies. Through optimizing the concentration of point defects and line defects, the carrier concentration and electrical conductivity were enhanced, yielding a much-improved power factor

of 5.3×10^{-4} W m^{-1} K^{-2} at 823 K; lattice thermal conductivity was significantly reduced by enhanced phonon scattering. A low, temperature-stable thermal conductivity of 2.6 W m^{-1} K^{-1} was achieved, leading to a *ZT* value of 0.17 at 873 K for compositions with $x = 0.06$; the highest *ZT* value reported for single Nb-doped TiO_2 ceramics without the use of SPS. We demonstrate the control of thermoelectric properties of Nb-doped TiO_2 ceramics through the development of balanced defect structures, which could guide the development of future oxide thermoelectric materials.

KEYWORDS: Thermoelectric, Nb doping, Magnéli, oxygen vacancies, twin boundaries

INTRODUCTION

Thermoelectric (TE) materials are able to directly convert heat energy into electrical energy, offering routes to contribute to energy sustainability and global environmental changes. The evaluation of a materials' TE performance is usually based on the dimensionless figure of merit, $ZT = \frac{S^2\sigma}{k}T$, where S is the Seebeck coefficient, σ is electrical conductivity, κ is thermal conductivity and T is the absolute temperature. To improve the TE performance and increase *ZT* of a candidate material, the power factor ($S^2\sigma$) needs to be enhanced and/or thermal conductivity needs to be reduced, but coupling effects between the TE parameters makes this challenging. Considerable efforts have been made to maximize *ZT* values; however, current commercial TE materials are predominantly based on rare, expensive and toxic elements, which hinders worldwide exploitation. Consequently, there is a growing demand for readily available, low cost, environmentally-friendly thermoelectric materials.

Oxide materials based on earth-abundant elements exhibit exceptional chemical and thermal stability at high temperatures under oxidizing environments; they show considerable potential as candidates for high temperature TE applications[1–4]. A wide range of oxide thermoelectrics have been investigated; cobaltites (including $NaCo_2O_4$[5], $Ca_3Co_4O_9$[6], $Ca_2Co_2O_5$[7] and $Bi_2Sr_2Co_2O_y$[8]) are the most popular *p*-type TE materials. Amongst the corresponding *n*-type TE materials, $SrTiO_3$[9], $CaMnO_3$[10], donor doped TiO_2[11,12], Magnéli phases (Ti_nO_{2n-1}[13,14] and $Nb_{12}O_{29}$[1]), In_2O_3[4,15] and tungsten bronze structured oxides ($Ba_{5.19}Nd_{8.54}Ti_{18}O_{54}$[16] and $Ba_6Ti_2Nb_8O_{30}$[17]) show much promise.

TiO_2-based materials have been widely investigated for solar cell[18], photovoltaic[19] and photocatalytic applications[20]. For TE applications, rutile structured, TiO_2 ceramics are attractive because of the low cost of the raw materials and high temperature stability. However, the key obstacle to the exploitation of TiO_2 ceramics is their modest thermoelectric performance. In particular, the relatively high thermal conductivity (6-8 W m^{-1} K^{-1} for single crystal rutile[21] and 3-6 W m^{-1} K^{-1} for polycrystalline rutile[22]) and low electrical conductivity limit the *ZT* value, to typically less than 0.001 at 1000 K[22]. Many strategies have been developed to improve the TE performance of TiO_2-based ceramics, with donor doping the most common. Donors such as Nb, Al and Ta[11,12,23] can increase the carrier concentration and mobility through reducing carrier localization; the mass/radii differences between donors and matrix can also be useful to enhance phonon scattering and thus reduce thermal conductivity. The effects of introducing high densities of oxygen vacancies and Magnéli phases have also been investigated, since the resulting crystallographic shear planes can act as phonon scattering centers, whilst not affecting carrier transport[13,14,24–26]. A variety of complex synthesis routes have been employed to develop nanostructures, including urea combustion[27], sol-gel and high pressure and high temperature

(HPHT) methods[28]. Nevertheless, such complex synthesis methods can be expensive and are not ideal for large-scale application.

Guided by earlier work and using donor doping and a reducing atmosphere to control the type and concentration of defects, we present a facile, economical method to synthesize, in a single sintering step, *n*-type reduced, Nb-doped rutile structured TiO_2 with enhanced performance. We provide atom level details of Magnéli phases and shear structures. From a combination of dopants, oxygen vacancies and planar defects, the thermal conductivity was minimized. The charge transport properties were improved by a factor of two compared to pure rutile. We show the significant enhancement of *ZT* was a direct consequence of controlling the microstructure and defect structures of the material.

EXPERIMENTAL METHODS

Nb-doped TiO_2 thermoelectric ceramic samples were prepared by conventional mixed oxide route. The TiO_2 powder (Sigma Aldrich, >99.99%) and Nb_2O_5 powder (Sigma Aldrich, >99.99%) were vibration milled with Propan-2-ol (Fisher Scientific®) and YSZ balls (Pi-kem) for 24 hours. The mixtures were dried in air at 363 K for 24 hours then calcined in air in a covered alumina crucible at 1373 K for 4 hours. To lower the sintering temperature and increase sample density, 0.81wt% manganese (II) carbonate (Sigma Aldrich, >99.99%) powder was added to the calcined powders and then re-milled and dried once more. The final powder was pressed in a 20 mm diameter disk-shaped die under a pressure of 50 MPa. The cylindrical pellets were packed in, and surrounded by, carbon flakes (Sigma Aldrich, >99.99%) in a 30 mm diameter alumina crucible with alumina lid. The assembly was sintered in a box furnace at 1523 K for 8 hours. The carbon flakes created a reducing atmosphere; the large volume of flakes to

ceramic sample ensured that no more than 10% of flakes were consumed during each sintering run. The sample formulations and codes are listed in **Table 1**.

Table 1. Sample compositions and codes

Formulation: $(1-x)TiO_2 - xNb_2O_5$	Sample code
$x = 0.005$	TN5
$x = 0.010$	TN10
$x = 0.015$	TN15
$x = 0.030$	TN30
$x = 0.045$	TN45
$x = 0.060$	TN60

The crystal structure was analyzed using a Philips X'Pert X-ray diffractometer® (XRD) with Cu Kα radiation (λ = 1.540598 Å). Diffraction patterns were collected from 0° to 100°, with 0.033° step size. The lattice parameters were refined using Bruker *TOPAS* software. The microstructures were examined using a TESCAN MIRA LC FEG scanning electron microscope (SEM) equipped with an Oxford Instrument SDD energy dispersive X-ray (EDS) detector and an Oxford Instrument Symmetry electron backscattered diffraction (EBSD) detector.

Specimens for TEM analysis were prepared by standard crushing and Focused Ion Beam (FIB) techniques. For the crushing methods, fragments were ground in an agate mortar and pestle dispersed in chloroform/ Propan-2-ol and dropped onto a holey carbon grid. FIB specimens were prepared using an FEI FEG Quanta 3D Dual Beam Focused Ion Beam system equipped with both FEG SEM column and a Ga ion source FIB column. Phase identification employed a 200 kV FEI Tecnai 20 analytical LaB6 TEM. The nano-scale structures were identified using high-

resolution transmission electron microscopy (HRTEM) and scanning transmission electron microscopy (STEM), which were conducted with a 300 kV FEI Tecnai F30 analytical FEG TEM and a 200 kV Thermo Fisher Talos F200X FEG TEM equipped with a HAADF STEM detector and a Super-X EDXS detector. Atomically-resolved STEM images were acquired using an aberration-corrected dedicated scanning transmission electron microscope (100 kV Nion UltraSTEM100) equipped with high, middle, low-angle annular dark-field (HAADF, MAADF and LAADF) and an annular bright-field (ABF) STEM detectors. Crystal structure models, SAED pattern simulations and PXRD simulations were performed using *CrystalMaker* software. The element valence states were investigated by X-ray photoelectron spectroscopy (XPS) using High-Throughput XPS, ESCA2SR spectrometer (Scienta Omicron) with monochromatic Al Kα radiation (E_{source} = 1486.69 eV). Survey scans were conducted at 0-1200 eV (binding energy). Higher resolution scans were recorded for Ti (2p) peaks, Nb (3d) peaks, O (1s) peaks and C (1s) peaks. Carbon (1s) peaks (284.8 eV) were used to calibrate the binding energy for all the spectra. *CasaXPS* software was used to process and analyze the XPS data.

The transport properties, Seebeck coefficients and electrical conductivity were determined using an Ulvac-Riko ZEM-3 operating in low pressure He atmosphere from room temperature to 873 K. Hall effect measurements were carried out at room temperature using a Physical Properties Measurement System (PPMS; Quantum Design) under an applied magnetic field from -7 T to 7 T. Thermal conductivity was determined from density (ρ), thermal diffusivity (α) and heat capacity (C_p) values. Density was determined from mass and dimension measurements. Thermal diffusivity was measured by NETZCH LFA-427 in an Ar atmosphere from room temperature to 873 K. Heat capacity values were obtained by a NETZCH STA 449C in an Ar atmosphere from room temperature to 873 K.

RESULTS AND DISCUSSION

Bulk Property and Phase Analysis. All the sintered bulk samples were of high density (>97% theoretical), dark grey in color with no visible cracks. The relative density decreased with increasing Nb content (**Table S1** in Supporting Information (SI)).

X-ray Diffraction spectra for the final calcined powders are shown in **Figure S1a**; they are predominantly tetragonal (Space Group $P4_2/mnm$) TiO_2 rutile phase. For powders containing lower contents of Nb (TN5 to TN15), all peaks matched the TiO_2 rutile phase. For powders containing higher content of Nb, there were additional peaks, which corresponded to $TiNb_2O_7$ (Space Group $A1_2/m1$). The intensities of the new peaks increased with the increasing Nb content, as the amount of the new phase increased.

XRD patterns for the Nb-doped TiO_2 ceramics are shown in **Figure 1**; they are dominated by tetragonal TiO_2 rutile (Space Group $P4_2/mnm$). In contrast to the spectra for the calcined powders for TN5, TN10 and TN15 (samples with lower Nb contents), new, high intensity peaks appeared close to the peaks for (110) and (011) at 2θ values of 26.9°, 28.02°, 28.40°, 35.4° and 35.9°; the intensity reduced with the increasing Nb content. These peaks do not match existing phases in the standard database; their origin will be discussed in the TEM section. However, in the spectra for TN30, TN45 and TN60 (samples with higher Nb contents), there is almost no trace of these unknown peaks (**Figure 1b**). Refined lattice parameters for the main rutile phase (**Table 2** and **Figure S2**) increased with increasing Nb content, reflecting the expansion of the unit cell as Nb^{5+} (R_{Nb}^{5+}=0.64 Å) substituted for the smaller Ti^{4+} (R_{Ti}^{4+}=0.605 Å) ions[29].

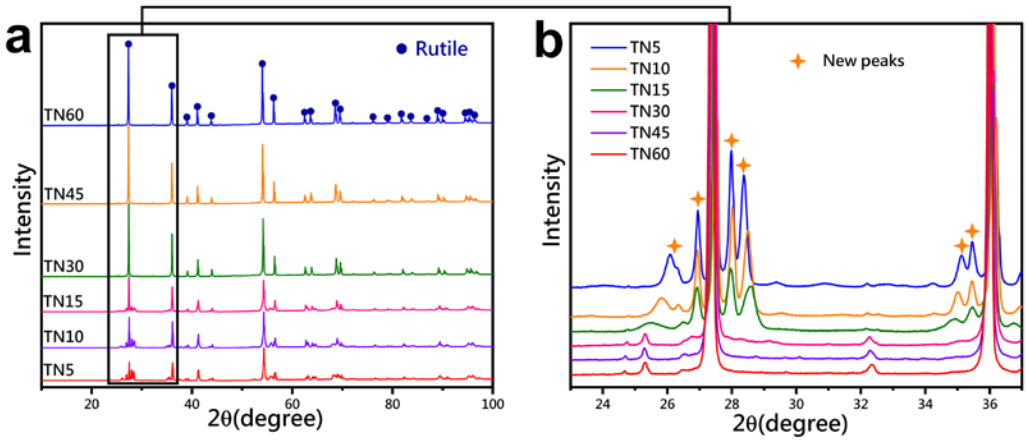

Figure 1. (a) XRD patterns for the sintered samples; (b): Enlarged view of the region from 23° to 37° in Figure (a).

Table 2. Lattice parameters for the rutile phase in Nb-doped TiO_2 ceramics

Sample	TN5	TN10	TN15	TN30	TN45	TN60
a, *b* (Å)	4.5955	4.5980	4.5994	4.6055	4.6125	4.6210
c (Å)	2.9570	2.9603	2.9629	2.9655	2.9685	2.9714

Scanning Electron Microscopy. SEM Back-Scattered Electron (BSE) images of Nb-doped TiO_2 ceramics are shown in **Figure 2**. All samples exhibit regular polygonal-shaped grains; average grain sizes varied between 7-13 μm, with a minimum for mid-range compositions of TN15 and TN30. (**Figure S3** and **Figure S4** show EBSD band contrast maps and grain size distributions). For samples TN5, TN10 and TN15, twin boundaries (marked with yellow dash lines) are present inside the grains, with rotation angles of approximately ~55° (TN5 - **Figure 2b**) and ~66° (TN10 - **Figure 2d**) respectively. A high density of wavy-shaped, domain structures are distributed inside the grains and on both sides of the twin boundaries; the dark stripes alternate with bright stripes, with intervals from approximately 170 nm to 300 nm

(**Figure 2b, d, f**). The twin boundaries and domain structures were interlaced, forming a twining-domain net-shape, complex structure. For samples TN30, TN45 and TN60, such sub-grain features did not develop but the concentration of pores increased. Some isolated micro-cracks occurred (marked with red arrows in **Figure 2a - i**), but the samples still exhibited high mechanical strength. In **Figure 2**, there is evidence of a secondary phase, bright in color at low levels of Nb, growing darker with increasing Nb content, segregating to the grain boundaries (circled blue in **Figure 2a - i**). EDS line analyses of the secondary phases (**Figure S5**) indicated they were enriched in Mn and contain almost no Nb, being very close to a mixture of TiO_2 and $MnTiO_3$. This may have originated from a low melting point eutectic between $MnTiO_3$ and TiO_2, promoting a liquid phase and sintering at a lower temperature[28]. BSE imaging and EDS analysis (**Figure S6** and **Figure S7**) showed no Ti or O segregation, but clear evidence of Nb segregation in samples with lower Nb contents (TN5-TN15); the darker grains are enriched with Nb while the lighter grains contain less Nb. High magnification EDS maps (**Figure S7**) for samples with lower Nb contents samples (e.g. TN10) indicated that the sub-grain features show the preference to grow in the lighter colored grains which have lower Nb content. By contrast, Nb is uniformly distributed inside the sub-grain domain structures, indicating that the sub-grain features do not affect the Nb distribution inside the grains. In samples with higher Nb contents (TN30-TN60), Nb is uniformly distributed inside the grains (**Figure S6**). The small dark areas represent Mn-rich secondary phases at the grain boundaries; the different levels of darkness are due to different grain orientations and not compositional differences.

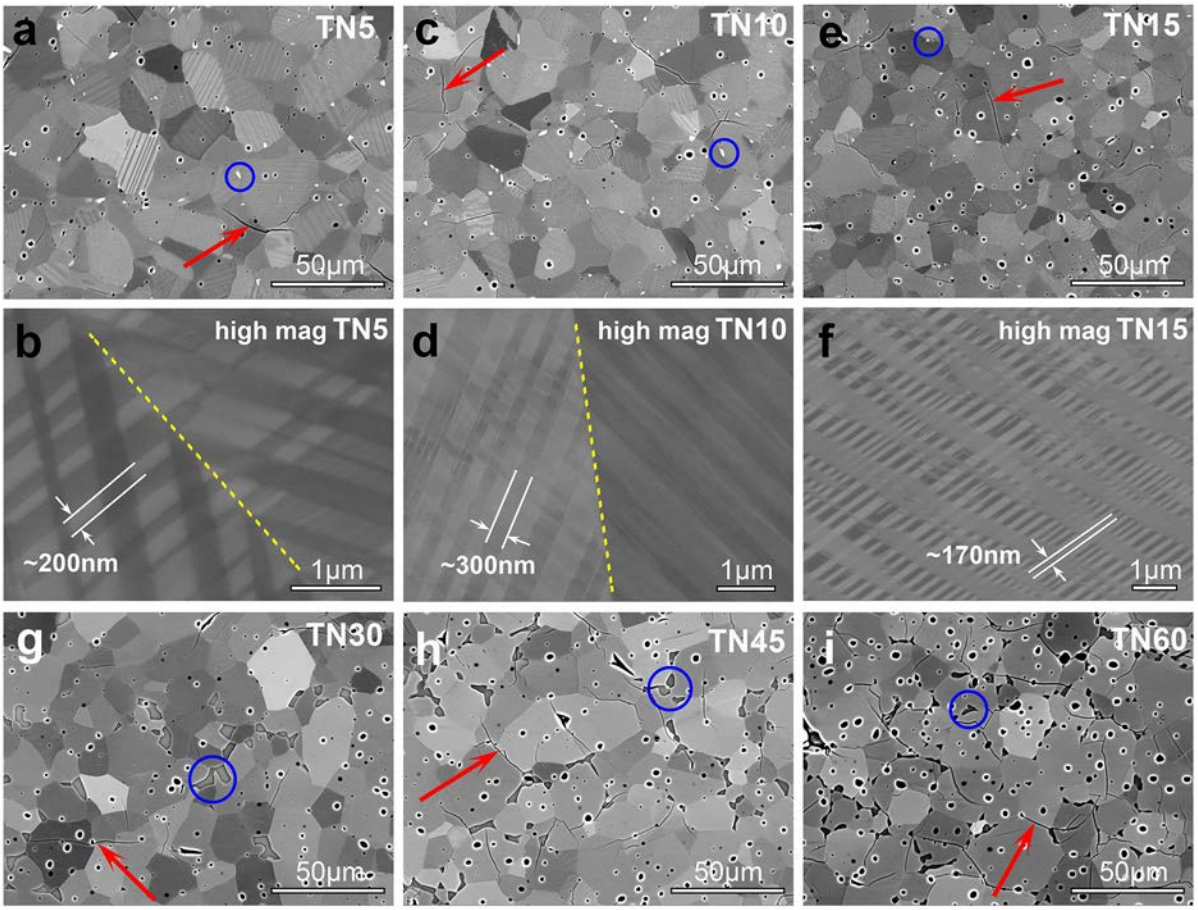

Figure 2. SEM Back-Scattered Electron (BSE) images of sintered TiO_2 samples: (a) TN5; (b) TN5 at higher magnification; (c) TN10; (d) TN10 at higher magnification; (e) TN15; (f) TN15 at higher magnification; (g) TN30; (h) TN45; (i) TN60.

Transmission Electron Microscopy. XRD and SEM analyses showed the Nb-doped TiO_2 ceramics are predominantly rutile phase with unknown secondary phases. TEM was employed to further investigate the crystal structures and microstructures. As samples TN5 to TN15 show similar XRD patterns and twin-domain structures, the TN15 sample was selected as the representative for this group. TEM selected area electron diffraction (SAED) patterns for TN15 along different rutile zone axes are shown in **Figure S8**; they confirm the existence of rutile structure, consistent with the XRD results. Twin defects are observed frequently in TN15. TEM

SAED patterns taken from twinned areas along $[010]_R$ and $[121]_R$ (R represents Rutile) zone axes are shown in **Figure S9a** and **Figure S9c**, with the corresponding simulated SAED patterns in **Figure S9b, Figure S9d**. The blue and red circles mark the reflection spots of the two sets of twin domains; the yellow circles identify typical reflection spots for (101) and (-101) twin planes. The rotation angle of the $\{101\}_R$ common twin plane is approximately 114 degrees[30,31]. In contrast, SEM images of the twin boundaries in TN15 (**Figure 2b** and **2d**) showed a rotation angle of approximately 55 degrees, indicating the twinning plane should be the $(310)_R$ plane[30]. In addition, anti-phase boundaries (APBs) were observed in TN15 samples (**Figure S10**); there was a high-density of boundaries with intervals of about 5-30 nm. The APBs can act as phonon scattering centers and help reduce thermal conductivity[32].

Single grain, TN15 TEM samples were prepared by FIB techniques. In the TEM bright field image (**Figure S11a**) there is a high density of net-shaped, domain-like nanostructures. An enlarged view of the region, denoted by the blue rectangular box in **Figure S11a,** is shown in **Figure S11b**. A SAED pattern collected from area A (circled in red in **Figure S11b**) along the $[1\text{-}11]_R$ zone axis, is shown in **Figure S11c**. The direction of the superlattice reflection spots point approximately along $(121)_R$. Since the interval of the superlattice reflection spots was approximately 13 times the inter-planar spacing, the Magnéli phase can be identified[23,24] as $Ti_{13}O_{25}$. To investigate the high n value (n>10) Magnéli phases such as $Ti_{13}O_{25}$, we collected SAED patterns from TN15 TEM samples prepared by standard crushing method. All diffraction patterns (**Figure 3**) were collected along $\langle 1\text{-}11 \rangle_R$ zone axis; the brighter reflection spots close to $(000)_R$ were identified as $(110)_R$, $(011)_R$ and $(121)_R$. The intervals of the superlattice reflection spots were approximately 12, 13, 14 and 16 times the inter-planar spacing, indicating the corresponding phases to be the $Ti_{12}O_{23}$, $Ti_{13}O_{25}$, $Ti_{14}O_{27}$ and $Ti_{16}O_{31}$ Magnéli phases with $\{121\}_R$

shear plane. In addition, HRTEM analyses indicated the existence of $Ti_{11}O_{20}$ Magnéli phase with $\{121\}_R$ crystallographic shear (CS) plane (**Figure S12**). As the $Ti_{12}O_{23}$ Magnéli phase with $\{121\}_R$ crystallographic shear plane was observed most frequently, we chose it as the representative phase and created a crystal structure model (**Figure S13a)**. Using this model for $Ti_{12}O_{23}$ Magnéli phase, we simulated XRD patterns for single phase $Ti_{12}O_{23}$ and the TiO_2/ $Ti_{12}O_{23}$ dual-phase system (**Figure S13b** and **Figure S13d**, respectively). From the XRD data for TN15 sample (**Figure 1**), three major peaks (close to $(110)_R$ peak) located at 26.9°, 28.02° and 28.4° and two major peaks (close to $(011)_R$ peak) located at 35.4° and 35.9° could not be identified using the standard database. Compared with the simulated patterns for the TiO_2/$Ti_{12}O_{23}$ dual-phase system, the three peaks close to the $(110)_R$ peak correspond well with the $(-121)_M$, $(1-21)_M$ and $(10-1)_M$ plane (M represents $Ti_{12}O_{23}$ Magnéli phase), and the two peaks close to the $(011)_R$ peak correspond well with the $(2022)_M$ and $(1023)_M$ plane (**Figure S13c** and **Figure S13d**). Therefore, from a combination of the XRD data and the experimental diffraction patterns, the major unknown peaks in the XRD pattern of TN15 appear to be from the $Ti_{12}O_{23}$ Magnéli phase. It should be noted that, in addition to the major $Ti_{12}O_{23}$ Magnéli phase, the SAED patterns indicated the presence of $Ti_{11}O_{20}$, $Ti_{13}O_{25}$, $Ti_{14}O_{27}$ and $Ti_{16}O_{32}$ Magnéli phases.

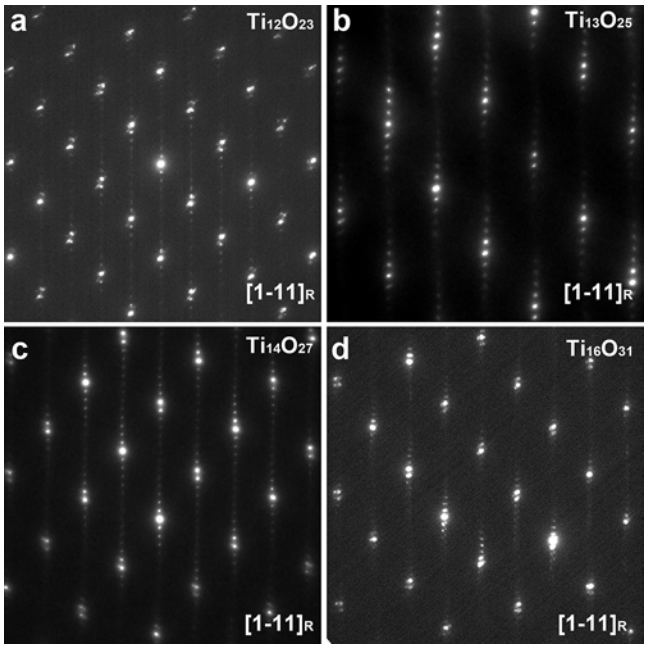

Figure 3. Experimental TEM selected area electron diffraction patterns for Magnéli phases along <1-11>$_R$ zone axis in TN15 sample: (a) $Ti_{12}O_{23}$; (b) $Ti_{13}O_{25}$; (c) $Ti_{14}O_{27}$; (d) $Ti_{16}O_{31}$.

STEM EDS was employed to examine the nanoscale chemical homogeneity of the net-shaped structure in TN15 (**Figure 4**). The TEM bright field image and SAED pattern indicate that the net-shaped structure contains $Ti_{13}O_{25}$ Magnéli phase (**Figure 4a**). The corresponding STEM HAADF image and EDS mapping analysis reveal the uniform distributions of Ti, Nb and O (**Figure 4b, d, e and f**), which are consistent with the SEM EDS results (**Figure S7**). HAADF STEM and corresponding FFT patterns of the region selected from **Figure 4b** (denoted by blue box) reveal that the interface is formed between the rutile phase (brighter area) and the high Magnéli phase (darker area) (**Figure 4c**). Atomically resolved STEM, in combination with HAADF, MAADF, LAADF and ABF, were used to define the atomic structure of the high order Magnéli phases (**Figure 5**). The HAADF and MAADF (MAADF STEM images provide better contrast for the CS planes) STEM images collected along <1-11>$_R$ reveal an ordered crystallographic shear (CS) structure, with the shear planes formed parallel to $\{121\}_R$ every

thirteen titanium planes (the interval of the shear planes being approximately 2.13 nm) (**Figure 5a** and **b**); the corresponding FFT patterns confirm that the interval of the superlattice reflection spots are 13 times the inter-planar spacing (**Figure 5c**), indicating the presence of $Ti_{13}O_{25}$ Magnéli phase with $\{121\}_R$ CS plane. Higher magnification HAADF and ABF STEM images reveal the $\frac{1}{2}[011]_R$ CS vector for $\{121\}_R$ CS plane (**Figure 5d** and **e**), which is consistent with the simulated $\{121\}_R$ CS interface along $<1\text{-}11>_R$ zone axis (**Figure 5f**). In addition, higher magnification LAADF and ABF STEM images indicate the presence of $\{10\text{-}1\}_R$ CS plane with $\frac{1}{2}[10\text{-}1]_R$ CS vector for $Ti_{10}O_{19}$ Magnéli phase along $<1\text{-}11>_R$ zone axis (**Figure 5g, h** and **i**). Based on earlier work of Magnéli phases[33–35], it is suggested that for Magnéli phases (Ti_nO_{2n-1}), the crystallographic shear slip planes are $\{121\}_R$ for $4 < n < 10$ and $\{132\}_R$ for $n > 10$. For samples of TN15 composition, this is the first atomic level observation of the complex high Magnéli phase (Ti_nO_{2n-1}, $n > 10$) with $\{121\}_R$ CS plane, plus definition of the atomic structure of the $Ti_{10}O_{19}$ Magnéli phase with $\{10\text{-}1\}_R$ CS plane for the first time. Therefore, the net-shaped structures were formed by the interlacing of different high Magnéli phases (Ti_nO_{2n-1}, $n \geq 10$) and the rutile phase.

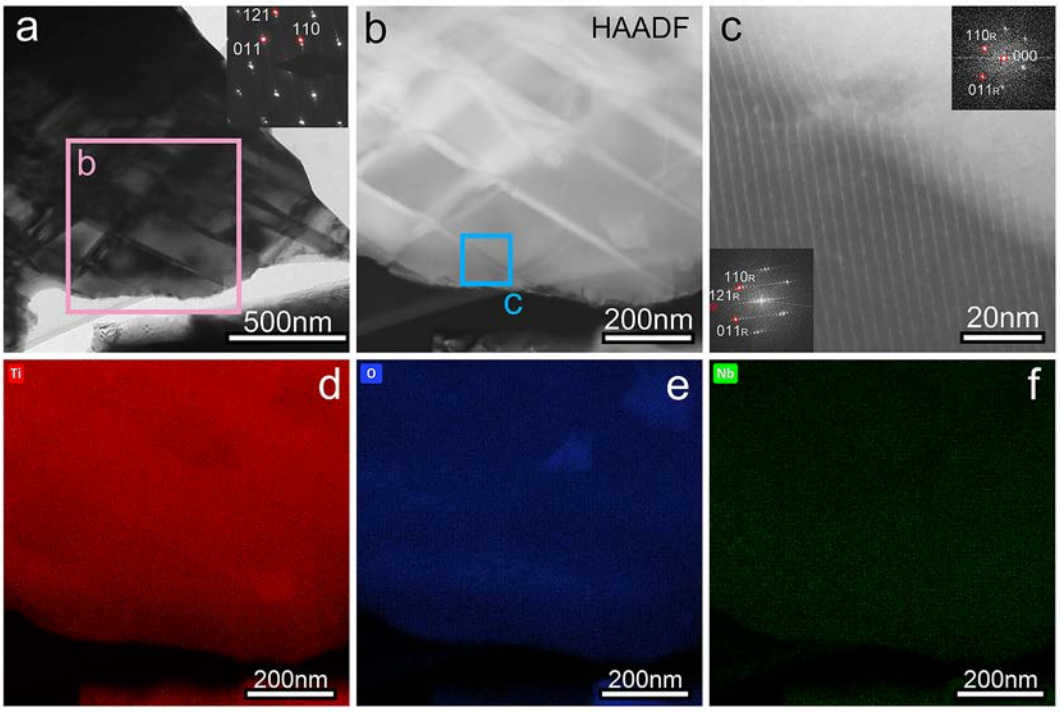

Figure 4. TEM analysis of TN15 sample: (a) TEM Bright field image of TN15 sample showing the sub-grain nanostructure and interfaces; the corresponding SAED pattern indicates the presence of a high Magnéli phase; (b) STEM HAADF image of region denoted by the pink box in (a); (c) Enlarged STEM HAADF image of region denoted by the blue box in (b) confirms the two different atomic structures; (d)(e)(f) STEM EDS mapping analysis of the region identified in (b).

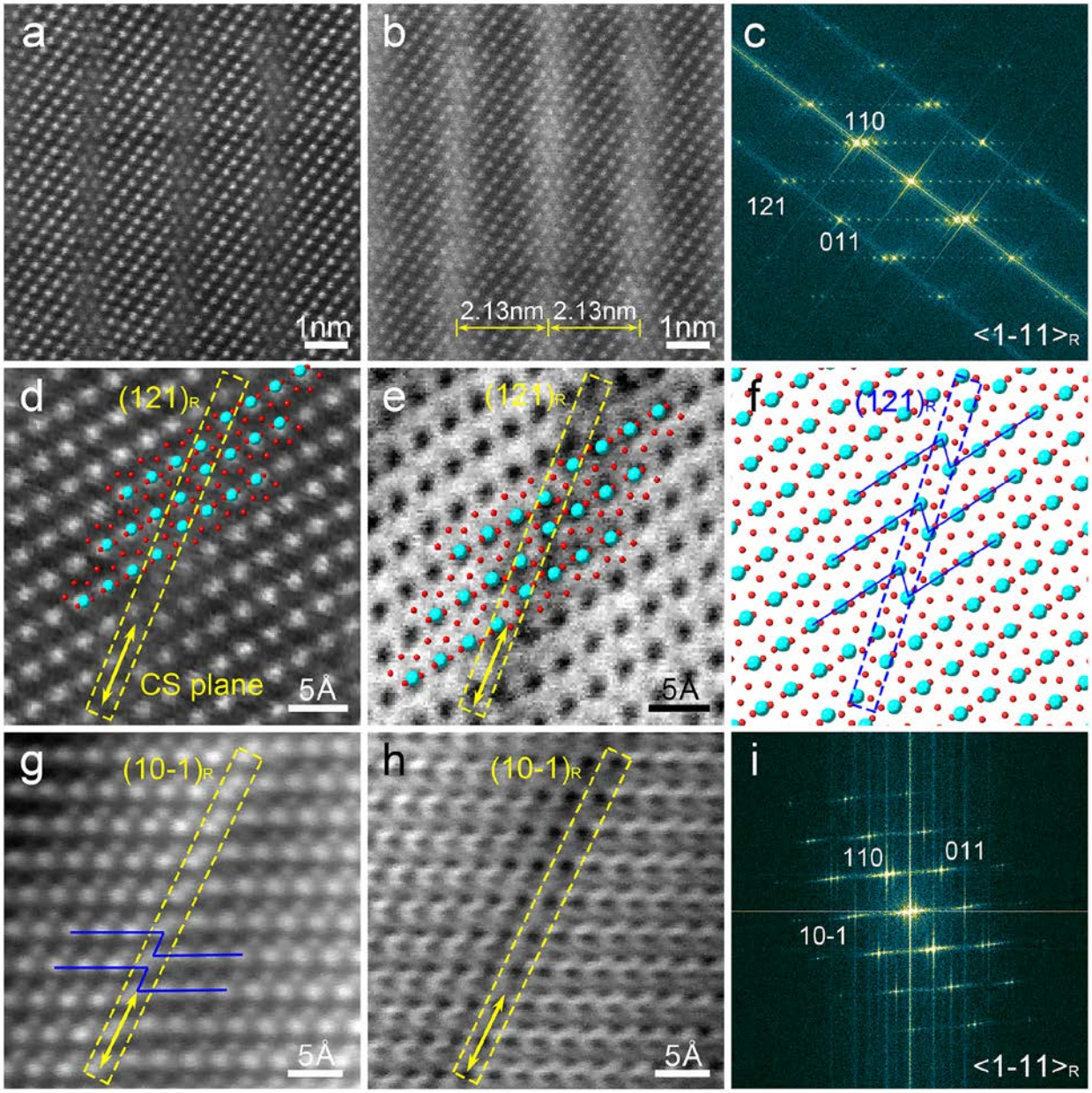

Figure 5. STEM analysis of the crystallographic shear structure in TN15 sample: (a) HAADF; (b) MAADF images acquired along <1-11>$_R$ zone axis; (c) Corresponding FFT pattern along <1-11>$_R$ zone axis; (d) HAADF and (e) ABF images of (121)$_R$ CS plane acquired along <1-11>$_R$ zone axis; (f) ball-and-stick models of (121)$_R$ CS structure along <1-11>$_R$ zone axis; (g) LAADF; (h) ABF images of (10-1)$_R$ CS plane acquired along <1-11>$_R$ zone axis; (i) corresponding FFT pattern along <1-11>$_R$ zone axis.

The Nb-doped TiO_2 ceramic samples with higher Nb contents (TN30 to TN60) exhibit similar XRD patterns and microstructures; TN60 was selected as representative for the structure of this group. The XRD data (**Figure 1**) and SEM micrographs (**Figure 2**) reveal no evidence of a secondary phase in TN60. TEM SAED patterns collected from different major zone axes ($[110]_R$, $[111]_R$ and $[0\text{-}10]_R$) for TN60 (**Figure S14**) confirm the sample is single phase rutile. HAADF and BF STEM images collected along $[101]_R$ and $[110]_R$ zone axes provide atomic-scale details of the TN60 structure (**Figure 6**), again consistent with that of rutile. In addition, HAADF and BF STEM indicate the presence of APBs along $[110]_R$ zone axis (**Figure 6c** and **d**), whilst TEM bright field and dark field images collected along the [11-3] zone axis reveal a high density of dislocations inside the rutile grain (**Figure S15**), which tends to lead to dislocation pile-up.

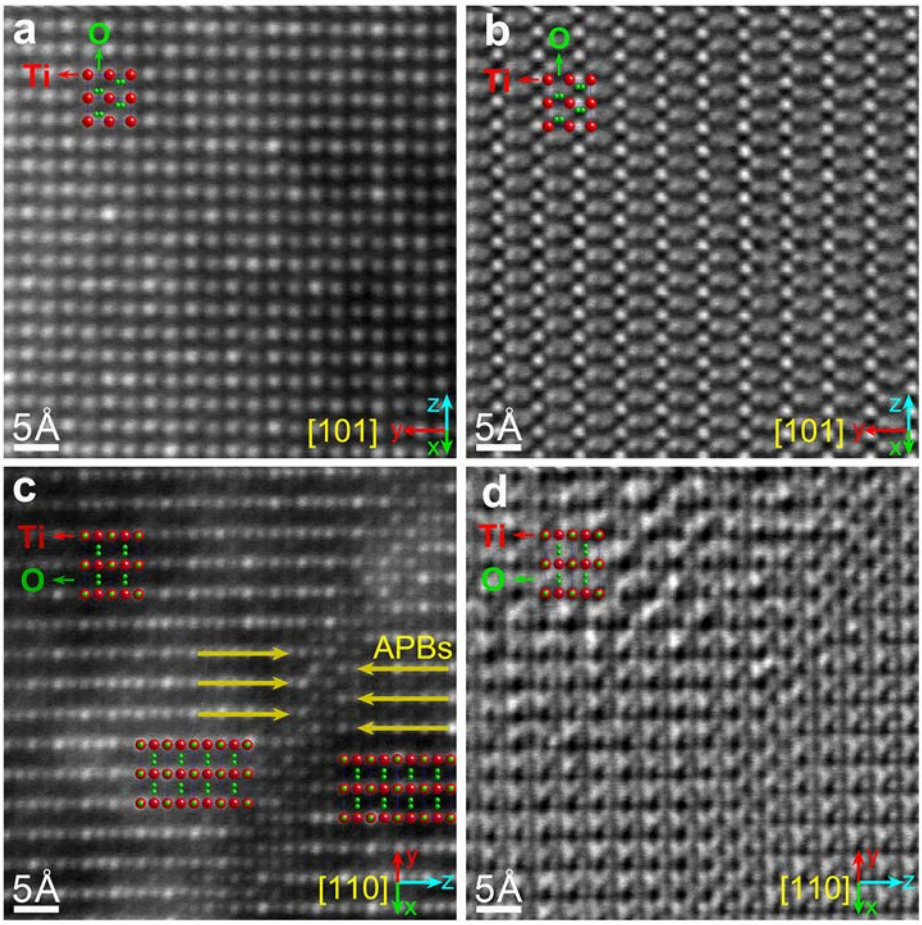

Figure 6. STEM analysis of TN60 samples (averaged by non-rigid registration from a stack of 20 consecutive frames): (a) HAADF and (b) BF images of TN60 sample along [101] zone-axis; (c) HAADF and (d) BF images of TN60 sample along [110] zone-axis. The ball-and-stick models are based on Rutile structure (where red balls denote Ti and the green balls denote O).

Twins can be frequently be observed in TN60 samples. **Figure 7a** is a TEM bright field image of TN60, showing two slender, needle-shaped twins inside the grain. **Figure 7b** and **Figure 7c** are the experimental and simulated SAED patterns obtained along the $<111>_R$ zone axis in **Figure 7a**, showing typical diffraction patterns for a twin structure[36–39]. The blue circles mark the reflection spots from the main twin domain, the red circles mark the reflection spots for a second twin domain, and the yellow circles mark the reflection spots of the (0-11) twin plane for

both twin domains. The reflection spots in the simulated SAED patterns match those in the experimental SAED patterns very well, although the intensities are different. This is because the twin domain volumes in the experimental samples are different, while the simulated SAED patterns were generated on the basis of twin domains having the same volume. The HRTEM image shown in **Figure 7d**, obtained from the region denoted by the yellow box area in **Figure 7a**, shows two nano-twins, approximately 7 nm and 1.5 nm wide. From the corresponding blue box and red box regions in **Figure 7d**, noise-filtered HRTEM images of the twins are presented in **Figure 7e** and 7**f**. The twin boundaries are indicated by the yellow dash lines, where the neighboring twin domains share the Ti(Nb) atoms at {0-11} twin boundaries. The neighboring twin domains are mirror symmetric to the {0-11} twin boundaries, and the rotation angle between the neighboring twin domains is 137 degrees, consistent with the work of Zheng *et al*[37] on twins in rutile-structured crystals. Zheng *et al.* suggested such twin boundaries can be called "coherent twin boundaries" (CTB), as there is no lattice misfit between the neighboring twin domains. **Figure 7f** represent twins with double CTBs; furthermore, we observed triple CTBs and even six CTBs inside the grains along the $<111>_R$ zone axis (**Figure 7h** and 7**i**). In addition, the TB can also co-exist with defects (**Figure 7g**). Since the intervals of these CTBs vary from 1-7 nm, which is about 2-10 times the size of the phonon mean free path for TiO_2 (0.8 nm), the twin boundaries can act also as phonon scattering centers. Earlier studies[40,41] demonstrated that twin boundaries can effectively scatter low energy carriers, without scattering the high energy carriers, so as to increase the Seebeck coefficient.

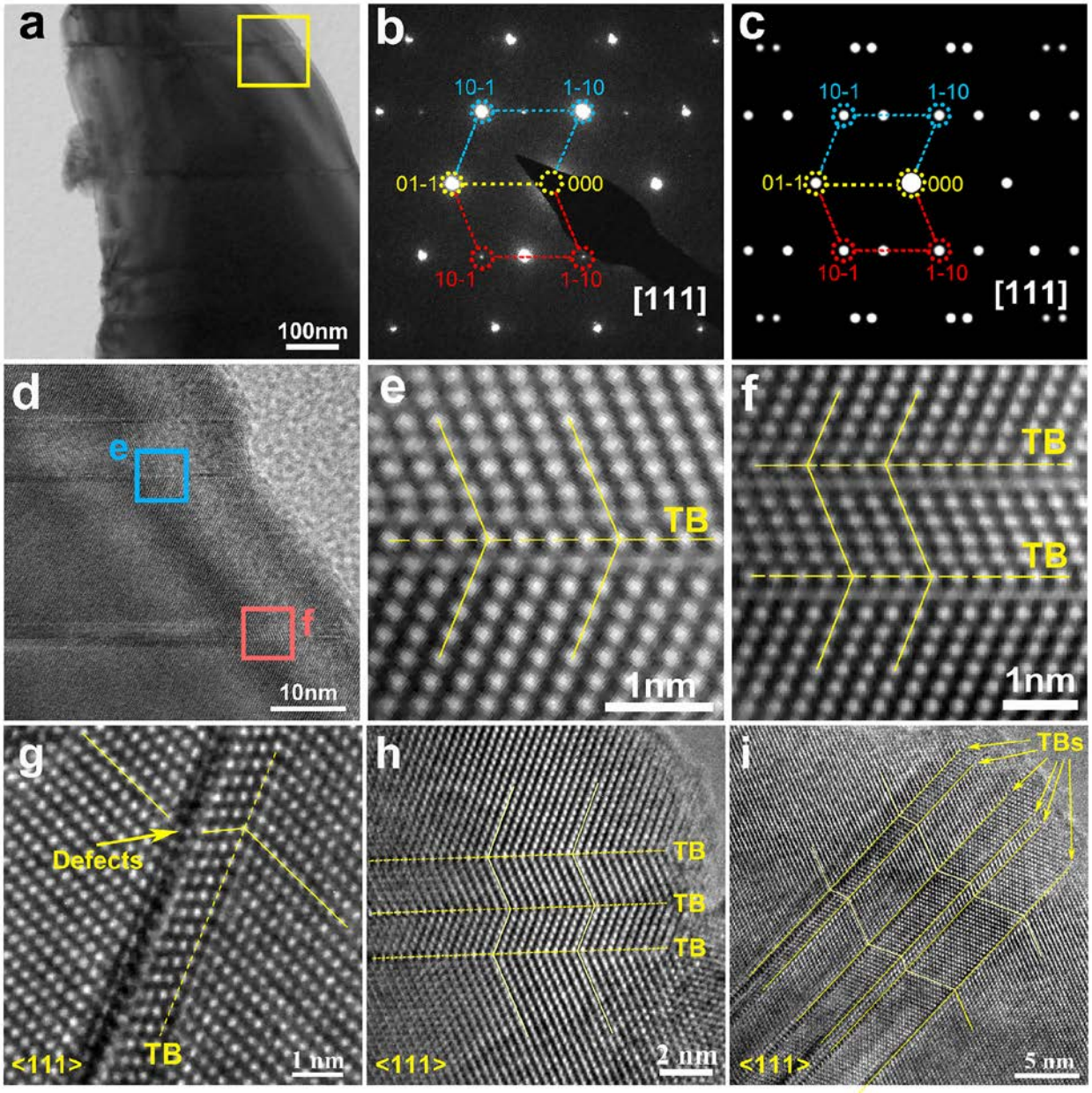

Figure 7. TEM analysis of TN60 samples: (a) TEM Bright field image of TN60 sample indicates the presence of nano-twins; (b) [111] zone-axis SAED pattern taken from the region denoted by the yellow box in (a); (c) simulated SAED pattern of (0-11) twins along [111] zone-axis; (d) HRTEM image taken from the region denoted by the yellow box in (a); (e) (f) noise-filtered HRTEM image from the blue box and red box regions in (d); (g) HRTEM micrograph of twin

boundaries with defects along <111> zone axis; (h) and (i) HRTEM micrographs of multiple twin boundaries along <111> zone axis in TN60 sample.

X-ray Photoelectron Spectroscopy. The valence states of the constituent elements were investigated by XPS. Survey scan spectra of the Nb-doped TiO_2 of different compositions (**Figure S16**) confirm the presence of all the constituting elements and the increasing Nb content from TN5 to TN60. High resolution Ti 2p and Nb 3d spectra are presented in **Figure 8**; calculated component data and peak position data from the spectra are presented in **Table 3** and **Table S2**. For Ti 2p spectra, the spin orbital splitting ($\Delta_{s.o.}$) of Ti $2p_{3/2}$ and $2p_{1/2}$ core levels is ~5.6 eV[41]. Asymmetries are observed for Ti 2p peaks, indicating the presence of both Ti^{4+} and Ti^{3+} states (TiO_2 and Ti_2O_3 spectra have different peak shapes)[43,44]. For all samples (TN5 to TN60), the [Ti^{3+}] content increases with increasing Nb doping (from 17.6% to 24.1%) (**Table 3**), indicating that higher Nb doping promotes the reduction process from Ti^{4+} to Ti^{3+}.

According to Di Valentin *et al.* [45], there are four types, or sources, of Ti^{3+} species in TiO_2, namely Ti^{3+} introduced by F- or Nb-doping, Ti^{3+}-OH associated with H-doping, Ti^{3+} introduced with oxygen vacancies, and interstitial Ti^{3+}. Two main Ti^{3+} species can be generated in our Nb-doped TiO_2 ceramics. The first is due to Nb doping; the Ti^{3+} ions can be generated by charge compensation (denoted as Ti^{3+}(d)). The other is under-coordinated Ti^{3+} species associated with oxygen vacancies generated by the reducing atmosphere treatment (denoted as Ti^{3+}(v)). The two Ti^{3+} species can be closely associated with the electrical conductivity by localized electrons, and will be discussed later in the transport property section.

For Nb3d spectra, the spin orbital splitting ($\Delta_{s.o.}$) of Nb $3d_{5/2}$ and $3d_{3/2}$ core levels is ~2.6 eV[46]. Asymmetry of the Nb 3d peaks also indicates the presence of both Nb^{5+} and Nb^{4+} states[47]. With increasing Nb content, the peak positions in all spectra are displaced to lower binding energy by

about 0.4 eV (from TN5 to TN60) (**Table 3**), and the [Nb^{5+}/Nb^{4+}] ratio is reduced, confirming the reduction of Nb.

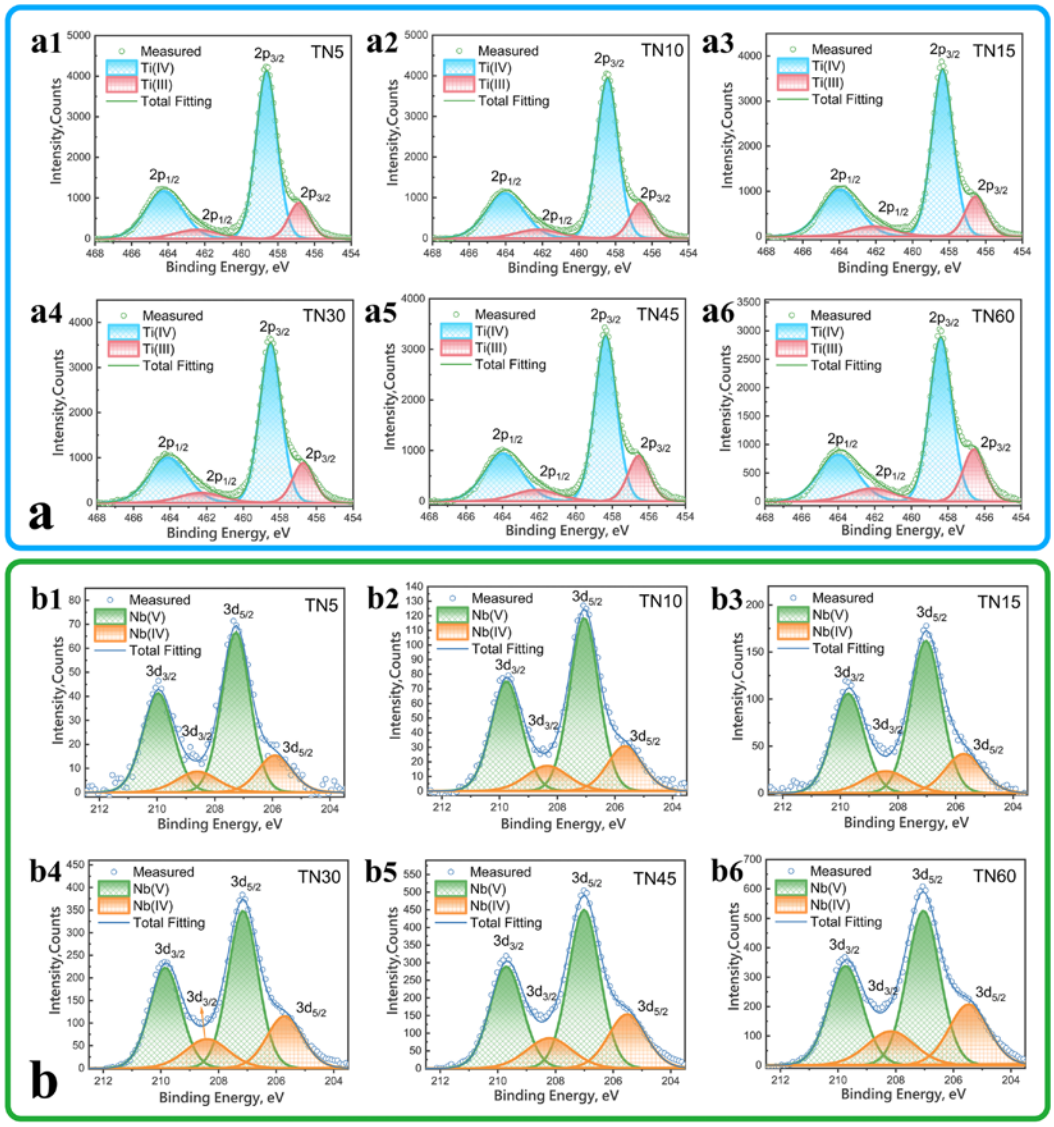

Figure 8. High resolution XPS spectra (a: Ti 2p transition; b: Nb 3d transition) for Nb-doped TiO_2 samples of different compositions: a1-a6 for TN5-TN60; b1-b6 for TN5-TN60

Table 3. Component Analysis of XPS Spectra for Nb-doped TiO_2 samples.

Sample Code	$Ti2p_{3/2}$%		$Nb3d_{5/2}$%	
	Ti^{4+}	Ti^{3+}	Nb^{5+}	Nb^{4+}
TN5	82.4	17.6	78.3	21.7
TN10	82.0	18.0	76.2	23.8
TN15	80.7	19.3	76.4	23.6
TN30	80.0	20.0	71.5	28.5
TN45	78.5	21.5	70.9	29,1
TN60	75.9	24.1	67.9	32.1

The formula $Ti_{(1-x)}Nb_xO_{(2-y)}$ can be used to describe the level of Nb doping and oxygen vacancies. The oxygen deficiency (*y*) arises through Nb doping and the use of the reducing atmosphere which generates oxygen vacancies during sintering. By charge compensation, the concentrations of $[Ti^{3+}]/[Ti^{4+}]$ and $[Nb^{5+}/Nb^{4+}]$ can be defined in terms of *y* for different levels of Nb (**Table 4**). For lower Nb content (TN5 to TN15), there is no significant change in *y* with increasing Nb content (values of 0.081to 0.083), indicating similar concentrations of oxygen vacancies, which helps to explain the very similar microstructures (TN5 to TN15). Therefore, the effective formula for such samples (TN5 to TN15) is approximately $Ti_{(1-x)}Nb_xO_{1.918}$. This is very close to $Ti_{12}O_{23}$ (equivalent to $TiO_{1.917}$), consistent with the XRD and TEM SAED results for TN15 (**Figure 1** and **Figure 3**). In contrast for higher Nb content samples (TN30-TN60), the *y* values decrease with increasing Nb content, indicating that higher levels of Nb can suppress the formation of oxygen vacancies, which is consistent with the modelling work of Wang *et al.*[48] on oxygen vacancy formation in Nb-doped rutile TiO_2.

Table 4. Values of *x* and *y* in the formula $Ti_{(1-x)}Nb_xO_{(2-y)}$ for Nb-doped TiO_2 samples

Values	TN5	TN10	TN15	TN30	TN45	TN60
x	0.01	0.02	0.03	0.058	0.086	0.113
y	0.083	0.081	0.082	0.073	0.068	0.069

Charge transport properties. The charge transport properties of Nb-doped TiO_2 ceramics are shown as a function of temperature in **Figure 9**. The electrical conductivity is significantly higher than for pure rutile (additional reference sample, this study), and increases with increasing temperature for all samples (**Figure 9a**); the rate of increase of electrical conductivity at a specific temperature increases with increasing Nb content. Near room temperature (323 K), the electrical conductivity initially increased with Nb doping, achieving a maximum for TN30, but then decreases with increasing Nb content. Hall Effect measurements undertaken at room temperature provide carrier concentrations and mobility values (**Table 5**). The carrier concentrations follow a similar trend to electrical conductivity, initially increasing with Nb content and then decreasing dramatically. In contrast, carrier mobility decreases from lower content samples (TN5 - TN15) to higher Nb content samples (TN30-TN60); this can be attributed to the combination of intrinsic effects (doping and point defects) and also extrinsic effects (grain and other boundaries). However, at elevated temperatures, the electrical conductivity increases continuously with increasing Nb content.

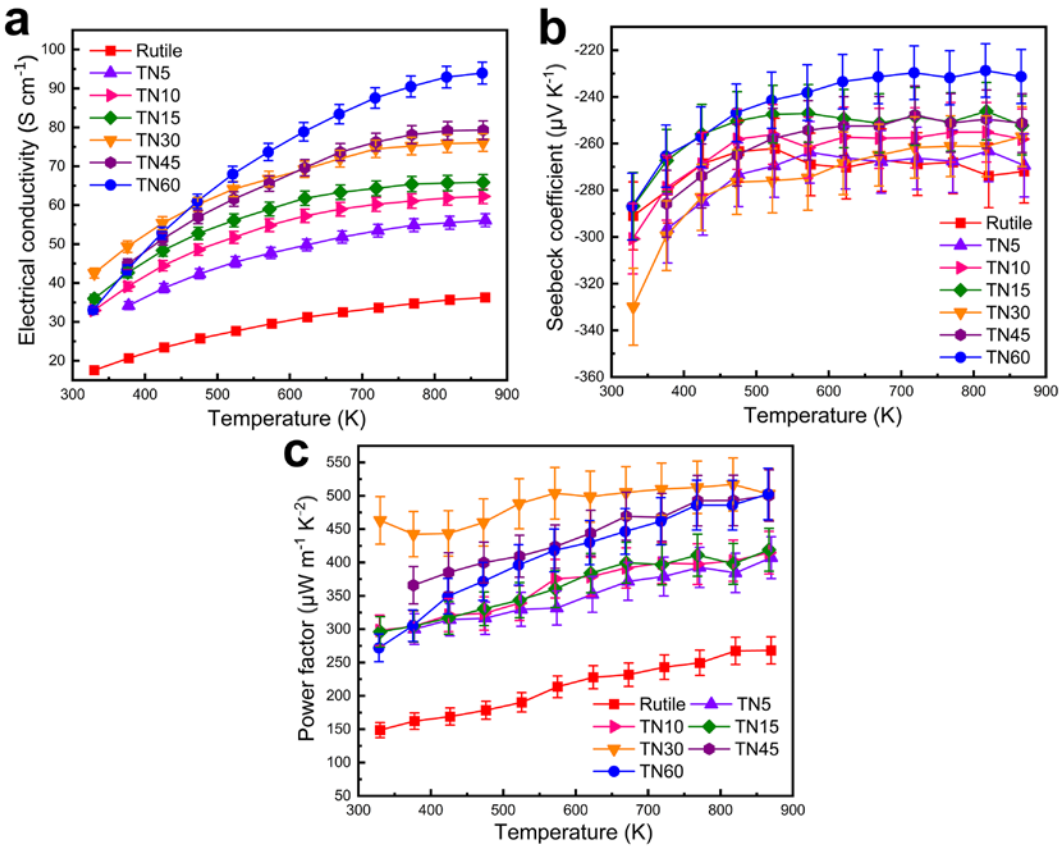

Figure 9. Transport Properties of Nb-doped TiO_2 ceramic samples as a function of temperature: (a) Electrical conductivity; (b) Seebeck coefficient; (c) Power factor.

Table 5. Electrical conductivity (σ), carrier concentration (n) and carrier mobility (μ) of the Nb-doped TiO_2 ceramics at room temperature

Sample	TN5	TN10	TN15	TN30	TN45	TN60
σ (S cm^{-1})	25.25	30.02	31.40	35.68	33.01	26.07
n (10^{20} cm^{-3})	0.575	1.480	3.100	12.00	4.950	6.260
μ (cm^2 V^{-1} s^{-1})	2.774	1.268	0.633	0.186	0.416	0.260

The trends for electrical conductivity at different temperatures can be explained in terms of the Ti^{3+} species. Near room temperature, the electrical conductivity of lower Nb content samples (TN5-TN15) can be attributed to the additional electrons introduced by Nb doping (related to Ti^{3+}(d)). However, from XPS (**Table 4**), the concentration of oxygen vacancies (related to Ti^{3+}(v)) starts to decrease from TN30. Recent studies[49,50] suggest that defect states induced by oxygen vacancies have strong localization effect on electrons. As the effect reduces (at TN30), the electrical conductivity and carrier concentration are maximized at room temperature. For samples with even higher Nb content (TN45, TN60), the electrical conductivity decreased steadily. The reciprocal Arrhenius plots indicate that the activation energy for conduction is increased for higher Nb content samples (**Figure S17**). According to earlier studies[51,52] for Nb-doped rutile TiO_2, the carriers tend to be self-trapped at Nb^{4+} sites at low temperatures. With increasing temperature, the carriers are partially thermally activated to Ti sites and form Ti^{3+}, and are eventually excited to the conduction band when enough energy is provided. Therefore, in the low temperature region, for higher Nb content samples, the higher content of Nb^{4+} and Ti^{3+} (**Figure 8b**) localizes more carriers, thereby significantly increasing the thermal activation energy. Furthermore, the shift of donor level towards the valence band with increasing Nb content has been confirmed by valence-band photoemission experiments[53]; the peak can further coalesce with the 4d peak of NbO_2, which supports the model that activation energy increases with higher Nb doping.

At elevated temperatures, the changes in electrical conductivity can be attributed to different localization effects produced by the reduced cations. Whilst electrons are ‘self-trapped’ on cation sites at low temperatures, the additional energy available at higher temperatures dominates processes, increasing carrier concentration and electrical conductivity.

The negative Seebeck coefficients (**Figure 9b**) confirm *n*-type behavior for the Nb-doped TiO_2 ceramics. With increasing temperature (from 323 K to 873 K) the absolute Seebeck coefficients decrease for all samples, reaching a minimum value of approximately ~230 μV K^{-1} for TN60 at 873 K, which is still higher than for many similar compositions[54–56]. However, the Seebeck coefficient of -330 μV K^{-1} for TN30, obtained near room temperature (323 K), is the highest value amongst the samples. Indeed, at elevated temperatures, the Seebeck coefficients for TN30 samples are still high, and second only to TN5. As carrier concentration increases with Nb content, there is the expected decrease in mobility (**Table 5**) as noted previously.

Through the combination of the highest Seebeck coefficients and electrical conductivity near room temperature, TN30 exhibits the highest power factor (470 μW m^{-1} K^{-2}) near room temperature (**Figure 9c**); this is the highest value reported for TiO_2-based materials without the use of SPS processing. For all samples, except TN30, the power factor increases with increasing Nb content. The highest power factor of 503 μW m^{-1} K^{-2} was achieved for TN60 sample at 873 K, approximately twice the value for pure rutile prepared in air/carbon atmosphere. The reproducibility of the power factor data is demonstrated in **Figure S18**, where data for sample TN60 are presented as an example.

Thermal Properties. The temperature dependences of the total thermal conductivity (κ_{total}) for Nb-doped TiO_2 ceramic samples are shown in **Figure 10a**; values range from 2.6 W m^{-1} K^{-1} to 4.4 W m^{-1} K^{-1}, and decrease with increasing Nb content and increasing temperature, reaching the lowest value of ~2.6 W m^{-1} K^{-1} for TN60 at 873 K. The collected κ_{total} values for these Nb doped samples are consistently lower than the thermal conductivity of single crystal rutile [21] (6-8 W/m K) and polycrystalline rutile[22] (4-5 W m^{-1} K^{-1}).

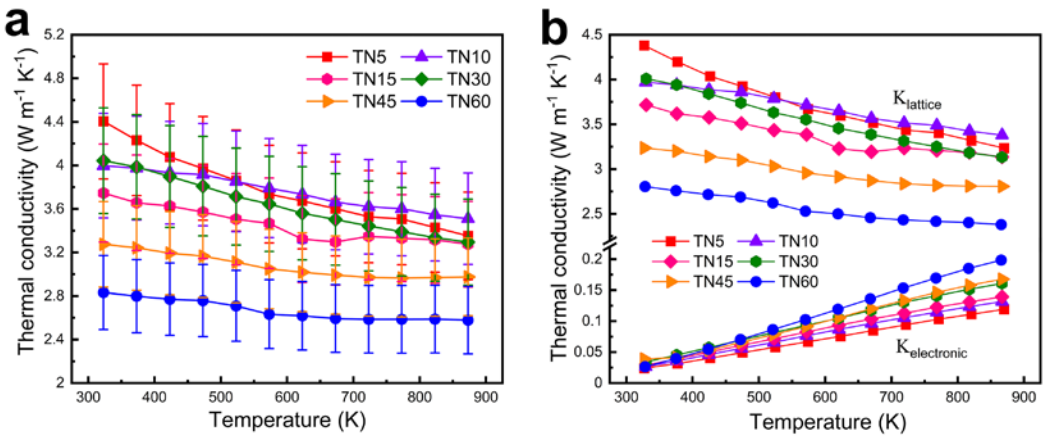

Figure 10. Temperature-dependent thermal conductivity of Nb-doped TiO_2 ceramic samples: (a) κ_{total} ; (b) $\kappa_{electronic}$ and $\kappa_{lattice}$.

By the Wiedemann–Franz approximation, ($\kappa_{total} = \kappa_{lattice} + \kappa_{electronic} = \kappa_{lattice} + L\sigma T$), the electronic and lattice thermal conductivity were determined as function of temperature (**Figure 10b**); L is the Lorenz factor ($L = 2.44 \times 10^{-8}$ J^2 K^{-2} C^{-2}), σ is electrical conductivity and T is temperature. The electronic components increase with increasing Nb content, reaching a maximum fraction of 7.7% of κ_{total} at 873 K for TN60. For all samples, lattice thermal conductivity is dominant and the changes in $\kappa_{lattice}$ as a function of both temperature and Nb content are consistent with those for κ_{total}.

The lattice thermal conductivity can be described by the Debye–Callaway model:

$$\kappa_L = \frac{K_B}{2\pi^2 v}\left(\frac{K_B T}{\hbar}\right)^3 T^3 \int_0^{\theta_D/T} \frac{\tau_C x^4 e^x}{(e^x-1)^2}\,\mathrm{dx} \qquad (1)$$

where K_B is the Boltzmann constant, υ is sound velocity, $\hbar$ is Planck's constant, θ_D is the Debye temperature, $x = \frac{\hbar\omega}{K_B T}$ is a dimensionless quantity, ω is the phonon frequency and τ_C is the overall relaxation time, which depends upon the phonon scattering processes operating[57] (**Equation S1 and S2**). Compared to pure TiO_2, the enhancement of phonon scattering in our material is mainly controlled by boundary scattering (grain boundaries, twin boundaries, anti-

phase boundaries and shear planes) and point defect scattering (dopants and vacancies). In samples with lower Nb contents (TN5-TN15), the presence of crystallographic shear structures (formed by the high density of oxygen vacancies) is one of the important factors for attaining lower lattice thermal conductivity. The Debye model (**Equation 2**) can be used to estimate the phonon mean free path from lattice thermal conductivity and sample density:

$$\kappa_{lattice} = \frac{1}{3} C_p \rho \upsilon l \qquad (2)$$

where C_p is the specific heat capacity, ρ is density, υ is sound velocity (6.91×10^{-3} m s^{-1} for rutile[58]) and l is phonon mean free path. For TN15 samples, the estimated phonon mean free path is approximately 0.52 nm at room temperature. This low value is mainly ascribed to the presence of crystallographic shear planes in the Magnéli phases (average CS spacing 1.65 nm to 2.13 nm), which are believed to contribute to phonon-boundary scattering and help reduce thermal transport[24,25]. The XPS data (**Table 4**) demonstrated that oxygen vacancy concentrations of samples with lower Nb contents (TN5-TN15) are essentially the same, and therefore the contributions to scattering by oxygen vacancies will be similar for TN5-TN15. Furthermore, the microstructures, and specifically grain sizes, of TN5-TN15 are not significantly different (**Figure S3** and **S4**). Therefore, the reduction in lattice thermal conductivity with increasing Nb doping level (from TN5 to TN15) can be attributed to increased scattering from point defects generated by Nb doping. The presence of the Nb, having different size and mass to the host atoms can introduce local strain-stress and mass fluctuations, which can effectively enhance the scattering of phonons of a particular wavelength. The fluctuations can be described by the Debye–Callaway model, as given by Klemense (details in Supplementary Information). Here the size and mass of Nb^{5+} (R_{Nb}^{5+} = 0.64 Å) are larger than those for Ti^{4+} (R_{Ti}^{4+} = 0.605 Å). According to **Equation S3, S4, S5 and S6**, the substitution of Nb ions for Ti ions will introduce significant local strain-

stress and mass fluctuations, increasing the disorder scattering parameter, promoting phonon scattering and reducing the overall relaxation time, and thus reducing lattice thermal conductivity. For higher Nb contents (TN30-TN60), the concentration of oxygen vacancies decreases with increasing Nb content (**Table 4**); therefore, the contribution of oxygen vacancies to the overall phonon scattering is reduced. However, lattice thermal conductivity decreases with increasing Nb content, which can be explained by the higher levels of point-defect scattering produced by the higher Nb doping.

Planar defect structures (twin boundaries and anti-phase boundaries) can also help to reduce lattice thermal conductivity by enhancing boundary scattering. It was noted that twin boundaries (TBs) are present inside the primary grains (**Figure 7** and **Figure S9**), and that TBs occur more frequently in samples with higher Nb content (e.g. TN60). The interval between the multiple TBs varies from 1 nm to 10 nm, which is about 1.5 ~ 15 times the phonon mean free path for rutile TiO_2. Again, these sizes are comparable with the phonon mean free path, implying that the TBs can effectively contribute to phonon scattering and thus help to reduce lattice thermal conductivity. Furthermore, a high density of dislocation was observed in TN60, which can similarly help to reduce thermal conductivity through phonon scattering[59,60].

Thermoelectric figure of merit (*ZT*). The resulting thermoelectric figure of merit, *ZT* values, for the Nb-doped TiO_2 ceramics are presented as function of temperature in **Figure 11a**. Whilst TN30 exhibits the highest power factor of 470 $\mu W\ m^{-1}\ K^{-2}$ at room temperature, the *ZT* value was only 0.04 due to the relatively high thermal conductivity; nevertheless, this is still the highest *ZT* value at room temperature. At elevated temperatures, the *ZT* values increase with increasing Nb content, to a maximum value of 0.17 for TN60 at 873 K. The *ZT* values from this study are presented graphically alongside data from other studies[1,12, 54–56,61] for single Nb-doped

TiO_2 based thermoelectric ceramics in **Figure 11b**. The present results show approximately 50% enhancement in *ZT* at 373 K compared with earlier studies. Indeed, the maximum *ZT* value obtained in this study (0.17, 873 K) is the equal to the highest reported *ZT* value for single Nb-doped TiO_2 ceramics, where the earlier samples were prepared by spark plasma sintering[1]. Furthermore, the maximum *ZT* values achieved in this study are comparable with Magnéli phase thermoelectric species[13,14,24]. Although marginally higher *ZT* values have been obtained for TiO_2 based thermoelectric ceramics, through a combination of more complex processing routes and co-doping, our approach is competitive and offers many advantages, not only because of the much simpler, easier and cheaper than alternative processing methods, but also because it provides a route and the potential for further enhancement of *ZT* values.

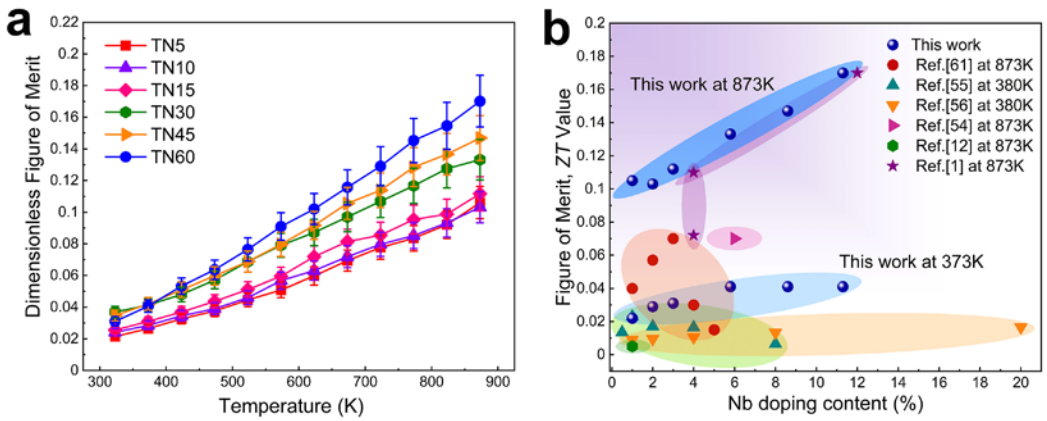

Figure 11. Thermoelectric figure for rutile-based ceramics: (a) results from this study (*ZT*) as a function of temperature; (b) compilation of *ZT* values for single Nb-doped, TiO_2-based thermoelectric ceramics.

CONCLUSIONS

High density, high quality Nb-doped TiO_2 thermoelectric ceramics were prepared by a single stage, mixed oxide route under air/carbon reducing atmosphere, without the need for high

pressure. Manganese carbonate additions led to the formation of a liquid phase during processing, enabling 150 K reduction of the sintering temperature.

Microstructures of samples prepared with low Nb content (TN5-TN15) are dominated by rutile phase and high Magnéli phases (Ti_nO_{2n-1}; $10 \leq n \leq 16$), which are interlaced to form net-shaped structures. We provide direct evidence for $\{121\}_R$ crystallographic shear planes in the high Magnéli phases and corresponding atomic resolution observations. In contrast, samples with high Nb content (TN30-TN60) were dominated by rutile phase with a high density of twin boundaries, anti-phase boundaries and dislocations; we present atomic level observations for twin boundaries and anti-phase boundaries in the rutile. High resolution XPS data showed that Nb doping can suppress the formation of oxygen vacancies.

By a combination of XRD, HREM and HRXPS we were able to define the structure of $Ti_{12}O_{23}$, the main high Magnéli phase, and provide detailed crystal structure and valence state evolution from the multi-phase materials (TN5-TN15) to the single phase (TN30-TN60) TiO_2-based ceramics.

With increasing Nb content, the electrical conductivity and power factor increased significantly, except for TN30; the highest power factor of 530 $\mu W\ m^{-1}\ K^{-2}$ was obtained for TN60 at 823 K. At room temperature TN30 exhibited a very high-power factor of 470 $\mu W\ m^{-1}\ K^{-2}$, the highest value reported for TiO_2-based materials without the use of SPS processing.

Through the use of Nb doping and a reducing atmosphere the samples contained considerable numbers of point defects and planar defects which contributed to phonon scattering, helping to reduce lattice thermal conductivity to a minimum of 2.6 $W\ m^{-1}\ K^{-1}$. Consequently, there was a 50% enhancement in the *ZT* value at room temperature and a maximum value of 0.17 at 873 K,

equal to the highest reported for single Nb-doped TiO_2 ceramics; other studies relied on SPS or chemical processing.

This work presents new understanding of the microstructural evolution of n-type TiO_2 and offers a simple, economical fabrication route to enhance the thermoelectric performance. The control of thermoelectric properties of TiO_2 achieved here by Nb doping through engineering the defect structures could guide the development of future oxide thermoelectric materials.

ASSOCIATED CONTENT

Supporting Information

The following supporting information is available free of charge.

Density data for Nb-doped TiO_2 ceramic samples; XRD spectra of mixed final powders after calcination; Lattice parameters for the main rutile phase in Nb-doped TiO_2 ceramics; SEM EBSD Band Contrast Maps of Nb-doped TiO_2 ceramics; Average grain sizes of Nb-doped TiO_2 ceramics; SEM EDS line and map analyses of Nb-doped TiO_2 ceramics of different Nb contents; Experimental TEM SAED patterns, BF images, DF images and HRTEM images for samples TN15 and TN60; Simulated unit cell model and XRD patterns for $Ti_{12}O_{23}$ Magnéli phase; XPS survey spectra and Positions of the different fitted peaks in the HR XPS spectra; Calculated activation energy of bulk Nb-doped TiO_2 ceramics; Scattering processes and relaxation times.
(PDF)

AUTHOR INFORMATION

Corresponding Author

*Email: Robert.Freer@manchester.ac.uk

Notes

There are no conflicts to declare.

ACKNOWLEDGMENT

The authors are grateful to the EPSRC for the provision of funding for this work (EP/H043462, EP/I036230/1, EP/L014068/1, and EP/L017695/1 acknowledged by R.F.). The work was also supported by the Henry Royce Institute for Advanced Materials, funded through EPSRC Grants EP/R00661X/1, EP/S019367/1, EP/P025021/1, and EP/P025498/1. We gratefully acknowledge the support from X-ray facilities in the Department of Materials in the University of Manchester. X.L thanks China Scholarship Council for their financial support during his Ph.D. program. All research data supporting this work are directly available within this publication.

REFERENCES

(1) Backhaus-Ricoult, M.; Rustad, J.; Moore, L.; Smith, C.; Brown, J. Semiconducting Large Bandgap Oxides as Potential Thermoelectric Materials for High-Temperature Power Generation? *Appl. Phys. A: Mater. Sci. Process.* **2014**, *116* (2), 433–470.

(2) Ohtaki, M. Recent Aspects of Oxide Thermoelectric Materials for Power Generation from Mid-to-High Temperature Heat Source. *J. Ceram. Soc. Jpn.* **2011**, *119* (1395), 770–775.

(3) Koumoto, K.; Wang, Y.; Zhang, R.; Kosuga, A.; Funahashi, R. Oxide Thermoelectric Materials: A Nanostructuring Approach. *Ann. Rev. Mater. Res.* **2010**, *40*, 363–394.

(4) Koumoto, K.; Funahashi, R.; Guilmeau, E.; Miyazaki, Y.; Weidenkaff, A.; Wang, Y.; Wan, C. Thermoelectric Ceramics for Energy Harvesting. *J. Am. Ceram. Soc.* **2013**, *96* (1), 1–23.

(5) Terasaki, I.; Sasago, Y.; Uchinokura, K. Large Thermoelectric Power in $NaCo_2O_4$ Single Crystals. *Phys. Rev. B.* **1997**, *56* (20), 12685–12687.

(6) Yu, J.; Chen, K.; Azough, F.; Alvarez-Ruiz, D. T.; Reece, M. J.; Freer, R. Enhancing the Thermoelectric Performance of Calcium Cobaltite Ceramics by Tuning Composition and Processing. *ACS Appl. Mater. Interfaces.* **2020**, *12* (42), 47634–47646.

(7) Funahashi, R.; Matsubara, I.; Ikuta, H.; Takeuchi, T.; Mizutani, U.; Sodeoka, S. Oxide Single Crystal with High Thermoelectric Performance in Air. *Jpn. J. Appl. Phys*. **2000**, *39* (11), p. 1127–1129.

(8) Combe, E.; Funahashi, R.; Azough, F.; Freer, R. Relationship between Microstructure and Thermoelectric Properties of $Bi_2Sr_2Co_2O_x$ Bulk Materials. *J. Mater. Res.* **2014**, *29* (12), 1376–1382.

(9) Ekren, D.; Azough, F.; Gholinia, A.; Day, S. J.; Hernandez-Maldonado, D.; Kepaptsoglou, D. M.; Ramasse, Q. M.; Freer, R. Enhancing the thermoelectric power factor of $Sr_{0.9}Nd_{0.1}TiO_3$ through control of the nanostructure and microstructure. *J. Mater. Chem. A.* **2018**, *6* (48), 24928–24939.

(10) Song, X.; Paredes Navia, S. A.; Liang, L.; Boyle, C.; Romo-De-La-Cruz, C. O.; Jackson, B.; Hinerman, A.; Wilt, M.; Prucz, J.; Chen, Y. Grain Boundary Phase Segregation for Dramatic

Improvement of the Thermoelectric Performance of Oxide Ceramics. *ACS Appl. Mater. Interfaces.* **2018**, *10* (45), 39018–39024.

(11) Xu, L.; Garrett, M. P.; Hu, B. Doping Effects on Internally Coupled Seebeck Coefficient, Electrical, and Thermal Conductivities in Aluminum-Doped TiO_2. *J. Phys. Chem. C.* **2012**, *116* (24), 13020–13025.

(12) Zaitsev, S. V.; Moon, J.; Takagi, H.; Awano, M. Preparation and Characterization of Nanocrystalline Doped TiO_2. *Adv. Powder Technol.* **2000**, *11* (2), 211–220.

(13) Liu, Y.; Yang, J.; Liu, Y.; Zheng, J.; Lee, W.; Shi, J.; Horlyck, J.; Xie, J.; Tay, Y. Y.; Tan, T. T.; Yu, D.; Mole, R.; McIntyre, G.; Zhang, C.; Toe, C. Y.; Waite, T. D.; Scott, J.; Wang, Y.; Wu, T.; Han, S.; Li, S. Manipulation of Planar Oxygen Defect Arrangements in Multifunctional Magnèli Titanium Oxide Hybrid Systems: From Energy Conversion to Water Treatment. *Energy Environ. Sci.* **2020**, *13* (12), 5080–5096.

(14) Portehault, D.; Maneeratana, V.; Candolfi, C.; Oeschler, N.; Veremchuk, I.; Grin, Y.; Sanchez, C.; Antonietti, M. Facile General Route toward Tunable Magnéli Nanostructures and Their Use as Thermoelectric Metal Oxide/Carbon Nanocomposites. *ACS Nano.* **2011**, *5* (11), 9052–9061.

(15) Bérardan, D.; Guilmeau, E.; Maignan, A.; Raveau, B. In_2O_3:Ge, a Promising *n*-Type Thermoelectric Oxide Composite. *Solid State Commun.* **2008**, *146* (1–2), 97–101.

(16) Azough, F.; Freer, R.; Yeandel, S. R.; Baran, J. D.; Molinari, M.; Parker, S. C.; Guilmeau, E.; Kepaptsoglou, D.; Ramasse, Q.; Knox, A.; Gregory, D.; Paul, D.; Paul, M.; Montecucco, A.; Siviter, J.; Mullen, P.; Li, W.; Han, G.; Man, E. A.; Baig, H.; Mallick, T.; Sellami, N.; Min, G.;

Sweet, T. $Ba_{6-3x}Nd_{8+2x}Ti_{18}O_{54}$ Tungsten Bronze: A New High-Temperature *n*-Type Oxide Thermoelectric. *J. Electron. Mater.* **2016**, *45* (3), 1894–1899.

(17) Jiang, D.; Ekren, D.; Azough, F.; Day, S. J.; Chen, K.; Mahajan, A.; Kepaptsoglou, D. M.; Ramasse, Q. M.; Reece, M. J.; Freer, R. The Structure and Thermoelectric Properties of Tungsten Bronze $Ba_6Ti_2Nb_8O_{30}$. *J. Appl. Phys.* **2019**, *126* (12).

(18) Tang, Y. B.; Lee, C. S.; Xu, J.; Liu, Z. T.; Chen, Z. H.; He, Z.; Cao, Y. L.; Yuan, G.; Song, H.; Chen, L.; Luo, L.; Cheng, H. M.; Zhang, W. J.; Bello, I.; Lee, S. T. Incorporation of Graphenes in Nanostructured TiO_2 Films via Molecular Grafting for Dye-Sensitized Solar Cell Application. *ACS Nano.* **2010**, *4* (6), 3482–3488.

(19) Wei, Q.; Hirota, K.; Tajima, K.; Hashimoto, K. Design and Synthesis of TiO_2 Nanorod Assemblies and Their Application for Photovoltaic Devices. *Chem. Mater.* **2006**, *18* (21), 5080–5087.

(20) Williams, G.; Seger, B.; Kamt, P. TiO_2-Graphene Nanocomposites. UV-Assisted Photocatalytic Reduction of Graphene Oxide. *ACS Nano.* **2008**, *2* (7), 1487–1491.

(21) Touloukian Y. S.; Powell R.W.; Ho C.Y.; Klemens P.G. *Thermophysical Properties of Matter - The TPRC Data Series*. Thermal Conductivity - Metallic Elements and Alloys, Vol. 1; New York: IFI/Plenum, 1970.

(22) Nam, W. H.; Lim, Y. S.; Kim, W.; Seo, H. K.; Dae, K. S.; Lee, S.; Seo, W. S.; Lee, J. Y. A Gigantically Increased Ratio of Electrical to Thermal Conductivity and Synergistically Enhanced Thermoelectric Properties in Interface-Controlled TiO_2-RGO Nanocomposites. *Nanoscale.* **2017**, *9* (23), 7830–7838.

(23) Backhaus-Ricoult, M.; Rustad, J. R.; Vargheese, D.; Dutta, I.; Work, K. Levers for Thermoelectric Properties in Titania-Based Ceramics. *J. Electron. Mater.* **2012**, *41* (6), 1636–1647.

(24) Harada, S.; Tanaka, K.; Inui, H. Thermoelectric Properties and Crystallographic Shear Structures in Titanium Oxides of the Magnèli Phases. *J. Appl. Phys.* **2010**, *108* (8).

(25) Fan, Y.; Feng, X.; Zhou, W.; Murakami, S.; Kikuchi, K.; Nomura, N.; Wang, L.; Jiang, W.; Kawasaki, A. Preparation of Monophasic Titanium Sub-Oxides of Magnéli Phase with Enhanced Thermoelectric Performance. *J. Eur. Ceram. Soc.* **2018**, *38* (2), 507–513.

(26) Mikami, M.; Ozaki, K. Thermoelectric Properties of Nitrogen-Doped TiO_{2-x} Compounds. *J. Phys.: Conf. Ser.* **2012**; *379* (1).

(27) Liu, C.; Miao, L.; Zhou, J.; Huang, R.; Fisher, C. A. J.; Tanemura, S. Chemical Tuning of TiO_2 Nanoparticles and Sintered Compacts for Enhanced Thermoelectric Properties. *J. Phys. Chem. C.* **2013**, *117* (22), 11487–11497.

(28) Liu, H.; Ma, H.; Su, T.; Zhang, Y.; Sun, B.; Liu, B.; Kong, L.; Liu, B.; Jia, X. High-Thermoelectric Performance of TiO_{2-x} Fabricated under High Pressure at High Temperatures. *J. Materiomics.* **2017**, *3* (4), 286–292.

(29) Shannon, R.D. Revised effective ionic radii and systematic studies of interatomic distances in halides and chalcogenides. *Acta Cryst.* **1976**, *32*, 751–767.

(30) Lu, W.; Bruner, B.; Casillas, G.; He, J.; Jose-Yacaman, M.; Farmer, P. J. Large Scale Synthesis of V-Shaped Rutile Twinned Nanorods. *Cryst. Eng. Comm.* **2012**, *14* (9), 3120–3124.

(31) Daneu, N.; Rečnik, A.; Mader, W. Atomic Structure and Formation Mechanism of (101) Rutile Twins from Diamantina (Brazil). *Am. Mineral.* **2014**, *99* (4), 612–624.

(32) Xiong, S.; Latour, B.; Ni, Y.; Volz, S.; Chalopin, Y. Efficient phonon blocking in SiC antiphase superlattice nanowires. *Phys. Rev. B: Condens. Matter Mater. Phys.* 2015, *91* (22), 224307.

(33) Anderson, J. S.; Hyde, B. G. On the possible role of dislocations in generating ordered and disordered shear structures. *J. Phys. Chem. Solids.* **1967**, *28* (8), 1393–1408.

(34) Zhang, Q.; Liu, W.; Zhou, Y.; Li, J.; Sun, T.; Liu, Q.; Ma, Y.; Wang, J.; Li, J.; Zhao, R.; Sui, Y.; Matsumoto, T.; Muroyama, N.; Yamano, A.; Harris, K. D. M.; Shen, Z. J.; Terasaki, O. Andersson-Magnéli Phases Ti_nO_{2n-1}: Recent Progress Inspired by Swedish Scientists. *Z. Anorg. Allg. Chem.* **2021**, *647*, 126–133.

(35) Bursill, L. A.; Hyde, B. G. Crystal Structures in the {132} Crystallographic Shear Family of Higher Titanium Oxides Ti_nO_{2n-1}. *Acta Crystallogr., Sect. B: Struct. Sci., Cryst. Eng. Mater.* **1971**, *27* (1), 210–215.

(36) Hrkac, V.; Wolff, N.; Duppel, V.; Paulowicz, I.; Adelung, R.; Mishra, Y. K.; Kienle, L. Atomic Structure and Crystallography of Joints in SnO_2 Nanowire Networks. *Appl. Microsc.* **2019**, *49* (1), 1–10.

(37) Zheng, J. G.; Pan, X.; Schweizer, M.; Zhou, F.; Weimar, U.; Göpel, W.; Rühle, M. Growth Twins in Nanocrystalline SnO_2 Thin Films by High-Resolution Transmission Electron Microscopy. *J. Appl. Phys.* **1996**, *79* (10), 7688–7694.

(38) Suzuki, K.; Ichihara, M.; Takeuchi, S. High-Resolution Electron Microscopy of Lattice Defects in TiO_2 and SnO_2. *Philos. Mag. A.* **1991**, *63* (4), 657–665.

(39) Shen, P.; Hwang, S.-L.; Chu, H.-T.; Yui, T.-F.; Pan, C.; Huang, W.-L. On the Transformation Pathways of Alpha-PbO_2-Type TiO_2 at the Twin Boundary of Rutile Bicrystals and the Origin of Rutile Bicrystals. *Eur. J. Mineral.* **2005**, *17* (4), 543–552.

(40) Yu, Y.; He, D. S.; Zhang, S.; Cojocaru-Mirédin, O.; Schwarz, T.; Stoffers, A.; Wang, X. Y.; Zheng, S.; Zhu, B.; Scheu, C.; Wu, D.; He, J. Q.; Wuttig, M.; Huang, Z. Y.; Zu, F. Q. Simultaneous Optimization of Electrical and Thermal Transport Properties of $Bi_{0.5}Sb_{1.5}Te_3$ Thermoelectric Alloy by Twin Boundary Engineering. *Nano Energy.* **2017**, *37*, 203–213.

(41) Mao, J.; Wang, Y.; Kim, H. S.; Liu, Z.; Saparamadu, U.; Tian, F.; Dahal, K.; Sun, J.; Chen, S.; Liu, W.; Ren, Z. High Thermoelectric Power Factor in Cu-Ni Alloy Originate from Potential Barrier Scattering of Twin Boundaries. *Nano Energy.* **2015**, *17*, 279–289.

(42) Armitage, D. A.; Grant, D. M. Characterisation of Surface-Modified Nickel Titanium Alloys. *Mater. Sci. Eng., A.* **2003**, *349* (1–2), 89–97.

(43) Jackman, M. J.; Thomas, A. G.; Muryn, C. Photoelectron Spectroscopy Study of Stoichiometric and Reduced Anatase TiO_2 (101) Surfaces: The Effect of Subsurface Defects on Water Adsorption at near-Ambient Pressures. *J. Phys. Chem. C.* **2015**, *119* (24), 13682–13690.

(44) Kurtz, R. L.; Henrich, V. E. UHV-Cleaved Single Crystal Ti_2O_3 ($10\bar{1}2$) by UPS and XPS. *Surf. Sci. Spectra.* **1998**, *5* (3), 182–185.

(45) di Valentin, C.; Pacchioni, G.; Selloni, A. Reduced and N-Type Doped TiO_2: Nature of Ti^{3+} Species. *J. Phys. Chem. C.* **2009**, *113* (48), 20543–20552.

(46) Atashbar, M. Z.; Sun, H. T.; Gong, B.; Wlodarski, W.; Lamb, R. XPS Study of Nb-Doped Oxygen Sensing TiO_2 Thin Films Prepared by Sol-Gel Method. *Thin Solid Films.* **1998**, 238–244.

(47) Darlinski, A.; Halbritter, J. Angle-Resolved XPS Studies of Oxides at NbN, NbC, and Nb Surfaces. *Surf. Interface Anal.* **1987**, *10* (5), 223–237.

(48) Wang, X.; Wang, F. H.; Shang, J. X.; Zhou, Y. S. Ab Initio Studies of Nb Doping Effect on the Formation of Oxygen Vacancy in Rutile TiO_2. *J. Phys. Chem. Solids.* **2012**, *73* (1), 84–93.

(49) Cho, E.; Han, S.; Ahn, H.-S.; Lee, K.-R.; Kim, S. K.; Hwang, C. S. First-Principles Study of Point Defects in Rutile TiO_{2-x}. *Phys. Rev. B: Condens. Matter Mater. Phys.* **2006**, *73* (19).

(50) Perevalov, T. v; Gritsenko, V. A. Electronic Structure of TiO_2 Rutile with Oxygen Vacancies: Ab Initio Simulations and Comparison with the Experiment. *J. Exp. Theor. Phys.* **2011**, *112* (2), 310–316.

(51) Frederikse, H. P. R. Recent Studies on Rutile (TiO_2). *J. Appl. Phys* **1961**, *32* (10), 2211–2215.

(52) Chester, P. F. Electron Spin Resonance in Semiconducting Rutile. *J. Appl. Phys.* **1961**, *32* (10), 2233–2236.

(53) Morris, D.; Dou, Y.; Rebane, J.; Mitchell, C.; Egdell, R.; Law, D.; Vittadini, A.; Casarin, M. Photoemission and STM Study of the Electronic Structure of Nb-Doped TiO_2. *Phys. Rev. B* **2000**, *61* (20), 13445–13457.

(54) Liu, C.; Miao, L.; Zhou, J.; Huang, R.; Tanemura, S. Bottom-up Assembly to Ag Nanoparticles Embedded Nb-Doped TiO_2 Nanobulks with Improved *n*-Type Thermoelectric Properties. *J. Mater. Chem.* **2012**, *22* (28), 14180–14190.

(55) Yuan, Z.; Gong, J.; Xu, S.; Li, Z.; Tang, G. Investigation of the Thermoelectric Properties of Reduced Nb-Doped $TiO_{2-\delta}$ Ceramics. *J. Alloys Compd.* **2017**, *710*, 778–783.

(56) Yuan, Z.; Li, Z.; Xu, S.; Ma, W.; Xu, J.; Tang, G. Thermoelectric Properties of Nb-Doped $TiO_{2-\delta}$ Ceramics Reduced at Elevated Temperature. *Ceram. Int.* **2017**, *43* (17), 15454–15458.

(57) Ren, G. K.; Lan, J. le; Ventura, K. J.; Tan, X.; Lin, Y. H.; Nan, C. W. Contribution of Point Defects and Nano-Grains to Thermal Transport Behaviours of Oxide-Based Thermoelectrics. *NJP Comput. Mater.* **2016**, *2* (1), 16023.

(58) McQueen, R. G.; Jamieson, J. C.; Marsh, S. P. Shock-Wave Compression and X-Ray Studies of Titanium Dioxide. *Science.* **1967**, *155* (3768), 1401–1404.

(59) Xin, J.; Wu, H.; Liu, X.; Zhu, T.; Yu, G.; Zhao, X. Mg Vacancy and Dislocation Strains as Strong Phonon Scatterers in $Mg_2Si_{1-x}Sb_x$ Thermoelectric Materials. *Nano Energy.* **2017**, *34*, 428–436.

(60) Chen, Z.; Jian, Z.; Li, W.; Chang, Y.; Ge, B.; Hanus, R.; Yang, J.; Chen, Y.; Huang, M.; Snyder, G. J.; Pei, Y. Lattice Dislocations Enhancing Thermoelectric PbTe in Addition to Band Convergence. *Adv. Mater.* **2017**, *29* (23), 1606768.

(61) Verchère, A.; Pailhès, S.; le Floch, S.; Cottrino, S.; Debord, R.; Fantozzi, G.; Misra, S.; Candolfi, C.; Lenoir, B.; Daniele, S.; Mishra, S. Optimum in the Thermoelectric Efficiency of

Nanostructured Nb-Doped TiO_2 Ceramics: From Polarons to Nb–Nb Dimers. *Phys. Chem. Chem. Phys.* **2020**, *22* (23), 13008–13016.

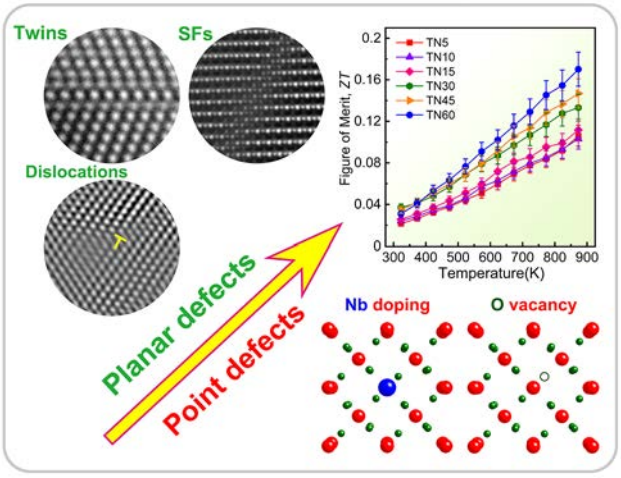
Twins
SFs
Dislocations
Planar defects
Point defects
TN5
TN10
TN15
TN30
TN45
TN60
Figure of Merit, ZT
Temperature(K)
0.2
0.16
0.12
0.08
0.04
0
300 400 500 600 700 800 900
Nb doping
O vacancy